

Time-Resolved Microscopy Analysis of Laser Photothermal Imaging Media

Hyunung Yu[†] and Dana D. Dlott[▲]

School of Chemical Sciences, University of Illinois at Urbana-Champaign, Urbana, Illinois 61801

E-mail: dlott@scs.uiuc.edu

F. Richard Kearney

Presstek, Inc., Hudson, New Hampshire 03051

Abstract. *Methods for understanding the fundamental mechanisms of laser photothermal imaging are described and applied to model imaging media. The light response is characterized with a series of Gaussian laser pulses of varying intensities and durations. The results are compared to a reference model, the “local fluence” model, that assumes the likelihood of exposure at a given pulse duration depends solely on the laser fluence received at that location. The mechanisms underlying the material behavior are studied with time-resolved microscopy using a variety of exposure and viewing conditions. The imaging media have in common a silicone rubber (polydimethylsiloxane) coating that can be removed by a single laser pulse to form an imaged spot that attracts ink. They differ in having a thin-film absorber layer, a volume absorber layer, or a combination of volume absorber and energetic underlayer. The thin-film media are the least sensitive with longer duration microsecond pulses but the most sensitive with nanosecond pulses, which is explained using a thermal conduction model. The volume absorbing media show deviations from the local fluence model that indicate the existence of useful dot gain properties which improve sensitivity. Time-resolved microscopy shows that this dot gain results from high-speed mechanical effects caused by hot gas trapped under a silicone rubber balloon. © 2006 Society for Imaging Science and Technology.*

[DOI: 10.2352/J.ImagingSci.Technol.(2006)50:5(401)]

INTRODUCTION

Laser photothermal imaging media exhibit an intrinsic non-linear (nonreciprocal) response to light. This response is the origin of two important properties, the insensitivity of these media to ambient light,^{1–5} and the sharp exposure threshold needed for digital imaging. However, a nonlinear response complicates the characterization and optimization of photothermal imaging media. We have studied photothermal imaging media in several previous works, where we introduced a time-resolved microscopy technique,^{6,7} made detailed measurements of the fluence threshold,⁸ studied the pulse duration dependence of this threshold,⁹ and investigated the effects of incorporating energetic materials.¹⁰ In the present work, we have made substantial improvements in the time-resolved microscopy technology that lets us watch the imaging process in real time with unprecedented detail. We have

combined this time-resolved microscopy technology with analysis techniques that involve detailed measurements of imaging thresholds using Gaussian profile laser pulses that span a wide range of pulse durations and pulse intensities, in order to investigate the fundamental mechanisms of photothermal imaging media. This powerful suite of analytical tools is well suited to elucidate the fundamental mechanisms of any laser-addressable imaging media, which is illustrated here using model systems that draw on elements used in Presstek, Inc.’s PEARL™ dry offset lithographic imaging technologies.^{8,11–13}

The techniques used here involve first measuring the size of imaged spots in sample media exposed to a series of imaging pulses of different intensities and durations.^{6,8–10,14,15} This information is used to determine a threshold fluence J_{th} that in general depends on the laser intensity and pulse duration. The measured thresholds are compared to a standard model termed^{10,16} the “local fluence model.” This model assumes that the likelihood of exposing any location within the laser beam depends solely on the fluence at that location. The actual results will no doubt deviate from this standard model when the intensity and duration are varied over a wide enough range. In the main, these deviations can be characterized as resulting from nonreciprocity or dot gain. Nonreciprocity means that the threshold depends not only on fluence, that is number of photons received per unit area, but also on intensity, that is the rate of photons received per unit area. Dot gain means that the imaged spot is larger than expected on the basis of the standard model. Dot gain with Gaussian profile pulses typically results from nonlocal effects that transfer some of the wasted energy at the beam center to the edges. Both nonreciprocity and dot gain can be exploited to improve the sensitivity of imaging media. An understanding of the fundamental mechanisms underlying these effects can be enhanced by time-resolved microscopy of the laser exposure process.⁶ High speed, stop-action images obtained with time resolution comparable to or better than the duration of the imaging pulse yield detailed information about the response of the imaging media to a laser,¹⁷ which provide feedback needed for systematic improvement of the imaging media.

It is also useful to understand how an imaging medium

[†]Present address: Korea Research Institute of Standards and Science, Daejeon 305-340 Korea.

[▲]IS&T Member

Received Aug. 1, 2005; accepted for publication Jan. 10, 2006.

1062-3701/2006/50(5)/401/10/\$20.00.

responds to a range of laser irradiation conditions,⁹ because there are many different types of imaging engines in use today with different laser intensities, pulse durations, spot sizes, etc. For instance one engine might use a bank of solid state diode lasers while another might use a single high power laser such as a fiber laser. Even if both engines deliver the same optical power (e.g., both engines deliver 30 W), the multibeam diode engine exposes materials to lower intensity longer duration pulses whereas the single beam engine exposes materials to higher intensity shorter duration pulses. Although this distinction would be unimportant for truly reciprocal materials such as silver halide films, the optimal design of a photothermal imaging material may be quite different for these radically different irradiation conditions.

In this paper three types of imaging media are investigated. One type denoted TF/A uses a thin-film absorber layer. A second type denoted V/A uses a volume absorber layer. The third type denoted V/A/E combines the volume absorber with an energetic underlayer. Here we focus on media response to laser beams having a Gaussian radial profile. Although this situation can be somewhat more complicated than top-hat beams with constant intensity profiles, many lasers deliver this type of beam. The optical engineering involved^{2,16} turns out to be not overly complicated. Furthermore, with a Gaussian beam, a medium is exposed to a wide range of intensities on a single laser shot, which provides a great deal of information.

The rest of this paper is organized as follows: (1) a model for the interaction of a medium with a Gaussian pulse; (2) a description of our time-resolved microscopy apparatus; (3) a description of the imaging media used here; (4) results of threshold measurements and time-resolved microscopy; (5) discussion; and (6) conclusion.

INTERACTIONS WITH GAUSSIAN BEAMS

In interpreting Gaussian exposure experiments we begin with a “local threshold approximation”^{10,16} reference model. Whether a given location becomes imaged is assumed to depend solely on whether or not that location received a threshold fluence J_{th} .

The laser pulse has a Gaussian spatial profile, characterized by a $(1/e^2)$ beam radius r_0 . Each single pulse irradiates the imaging medium with a range of fluences $J(r)$, that decreases radially outward from the beam center, as shown in Fig. 1(a). The pulse is usually characterized by a spatially averaged fluence parameter $J_{avg} = E_p / (\pi r_0^2)$, where E_p is the laser pulse energy. In terms of this parameter $J(r)$ is given by

$$J(r) = 2J_{avg} \exp\left(-\frac{2r^2}{r_0^2}\right). \quad (1)$$

Note the peak fluence at the beam center is exactly twice the average, $J(0) = 2J_{avg}$. Threshold measurements are made at fixed beam radius r_0 by exposing the medium to a succession of pulses having increasing energies E_p .^{2,6,15} Usually we use three pulses at each energy, which allows us to check for the possibility of an erroneous result due to laser flicker or media imperfections. At a critical value of E_p termed E_{th} ,

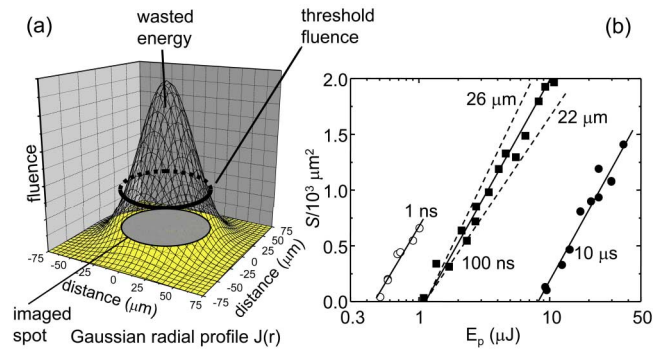


Figure 1. (a) A Gaussian radial profile pulse with radius $r_0 = 24 \mu\text{m}$, in combination with a sharp exposure threshold, produces imaged spots whose area S increase with pulse energy E_p above threshold. The darker region is the energy above threshold that is wasted. (b) Data obtained with Ti thin films on glass substrates at indicated pulse durations. In the local-fluence model the slope is equal to $\pi r_0^2 / 2$. The intercept with the x axis gives a threshold energy E_{th} . The dashed lines are used to estimate the error in determining r_0 .

the fluence $J(0)$ at the beam center exceeds J_{th} and an infinitesimal spot becomes exposed. Above E_{th} the spot size increases monotonically with pulse energy E_p . The exposed spot area S is a circular region [see Fig. 1(a)] with spot radius r_s ,¹⁰

$$S = \pi r_s^2 = 0, \quad J(0) < J_{th},$$

$$S = \pi r_s^2 = \frac{\pi r_0^2}{2} \ln \left[\frac{J(0)}{J_{th}} \right] = \frac{S_0}{2} \ln \left[\frac{J(0)}{J_{th}} \right], \quad J(0) \geq J_{th}, \quad (2)$$

where S_0 is a beam area parameter, $S_0 = \pi r_0^2$. Equation (2) shows that the exposed spot area grows logarithmically with increasing fluence above threshold. There are many tools for measuring laser pulse energy E_p , whereas determining fluence $J(r)$ or $J(0)$ is more complicated since both the energy and the beam profile must be known, so it is useful to write Eq. (2) in terms of E_p . Above threshold

$$S = \pi r_s^2 = \frac{S_0}{2} \ln \left(\frac{E_p}{E_{th}} \right) = \frac{S_0}{2} \ln \left(\frac{2E_p}{J_{th} S_0} \right). \quad (3)$$

Determining the exposure fluence by trying to find the fluence that makes an infinitesimal spot is not very accurate.¹⁸ Equation (3) shows that a plot of the exposed area S versus $\ln(E_p)$ should be linear. This line should cross the abscissa ($S=0$) at E_{th} . Thus it is better to determine E_{th} by measuring spot areas over a range of pulse energies and using linear least-squares methods to fit the data. With this method the determination of E_{th} acquires additional accuracy since it is determined not by a single measurement of an infinitesimal spot, but instead by extrapolation from many measurements of spots with finite areas.¹⁰ To convert E_{th} into J_{th} requires a knowledge of the beam area πr_0^2 . However, Eq. (3) shows that the slope of the line is $S_0 / 2 = \pi r_0^2 / 2$. Thus the threshold fluence,

$$J_{\text{th}} = E_{\text{th}}/\text{slope} = 2E_{\text{th}}/(\pi r_0^2), \quad (4)$$

is equal to the energy E_{th} where the line crosses the abscissa divided by the slope of the line.¹⁰

With media that obey Eqs. (2), there is a point of maximum efficiency.^{10,18} Imagine a beam focused to an area S_0 on an imaging medium. When $E_p \leq E_{\text{th}}$ then $S=0$ and there is no imaged spot, which is wasteful. As E_p passes through E_{th} , a spot appears and the imaged area S increases rapidly with increasing E_p . But when E_p is large enough, as shown by Eq. (3), S levels off and further large increases in E_p increase S only by small amounts, which is again wasteful. By taking the derivative of S with S_0 , the point of maximum efficiency is found to occur when $E_p = (e^1)E_{\text{th}} = (2.718\dots)E_{\text{th}}$ and $S = \pi r_0^2/2 = S_0/2$.¹⁸ At the point of maximum efficiency, the ratio of (wasted energy)/(total energy) is a minimum.

Figure 1(b) shows examples of data obtained with this technique, using a model imaging medium consisting of a ~ 30 nm layer of Ti sputtered onto a glass substrate. This simple imaging medium has previously been shown to behave ideally,^{10,19,20} in the sense that it accurately obeys Eq. (4) for pulse durations in the 10 ps–100 μs range. However, the imaging threshold J_{th} does depend a great deal on the laser intensity. At higher laser intensities, the media can be exposed by shorter duration pulses in such a manner that the exposure threshold fluences decrease as the pulse duration is reduced. Thus within this range the material evidences local but nonreciprocal behavior. Outside this range deviations from Eq. (4) can be observed. With pulses shorter than 10 ps, nonlinear optical effects come into play. With pulses longer than 100 μs , thermal conduction in the radial direction becomes important.

The Gaussian beam diameter has been determined through independent measurement, by scanning a razor blade across the focal plane, to be $r_0 = 24 \mu\text{m}$. At each pulse duration, the linear relation predicted by Eq. (4) is observed. The slope at each pulse duration is identical, but the intercept at E_{th} decreases markedly with decreasing pulse duration. A linear least-squares fit to the 100 ns data gives an area $S_0/2 = 893 (\pm 16) \mu\text{m}^2$, corresponding to a beam radius $r_0 = 23.9 (\pm 0.2) \mu\text{m}$. The bracketing lines in Fig. 1(b) indicate the sensitivity of this method to r_0 . The 100 ns threshold energy $E_{\text{th}} = 1.11 (\pm 0.05) \mu\text{J}$, giving a threshold fluence (100 ns) $J_{\text{th}} = 124 (\pm 6) \text{mJ}/\text{cm}^2$. Decreasing the pulse duration to 1 ns reduces the threshold by a factor of 2. Increasing the pulse duration to 10 μs increases the threshold by a factor of 7.

THRESHOLD MEASUREMENTS

Threshold measurements were made using a single-transverse mode Nd:yttrium-aluminum-garnet (YAG) laser at 1.064 μm wavelength. The pulse durations were 100 ns, 2.5, and 10 μs . The nanosecond pulses were generated using an intracavity Q switch. The microsecond pulses were generated using an extracavity pulse slicer. Pulse energies were measured with a pyroelectric Joule meter. To check the pulse energies, we also measured the laser power at a known rep-

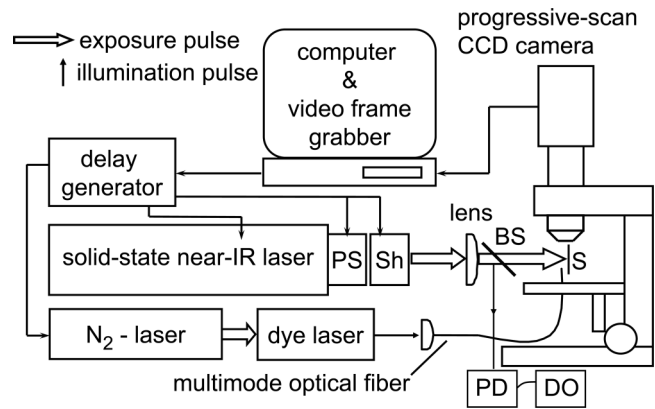


Figure 2. Block diagram of the time-resolved microscopy apparatus. BS: beam splitter; PD: photo diode; DO: digital oscilloscope; PS: pulse slicer; Sh: electronic shutter.

etition rate using a power meter. Samples were placed in the microscope and spots were imaged at a series of pulse energies. After cleaning the imaged samples with lens tissue wetted with methanol, the spot areas were measured by digital video microscopy.

MICROSCOPY APPARATUS

The microscopy apparatus diagrammed in Fig. 2 has been described previously,^{6,8,17} but we have introduced a few improvements worth mentioning. The previous version used a camera and frame grabber that supported only interlaced image acquisition. Since stop-action images are acquired in a single shot, one-half of the lines were blank which degraded the image quality. A new video camera (JAI CV-A11) and frame grabber (National Instruments NI PCI-1407) are now used that support noninterlaced images. Since this frame grabber also supports external triggering, the home built timing and delay generator was modified as well. The subnanosecond strobe pulse is transmitted to the microscope using a 100 μm diameter multimode optical fiber. The fiber makes it possible to change the position and intensity of the strobe pulse easily. Owing to this improvement, we have been able to evaluate a number of different exposure and detection schemes.

The stop-action images are acquired during a subnanosecond time interval which is determined by the strobe pulse duration. To obtain these, the following procedure was used. The near-infrared (IR) imaging laser at 1.064 μm , the N_2 -pumped dye-laser strobe at 500 nm, and the frame grabber are triggered at a repetition rate of 10 Hz. The delay generator chooses the near-IR pulse duration and the relative delay between the imaging and strobe pulses. There is a nanosecond time scale jitter between these two pulses. Although we cannot predict the exact time interval between pulses to better than a few tens of nanoseconds, we can measure this interval accurately by recording the pulses on a fast digital oscilloscope. An electronic shutter in the path of the imaging laser beam is closed. In the absence of imaging pulses, the imaging media can be positioned so that the strobe gives a high-quality image on the computer moni-

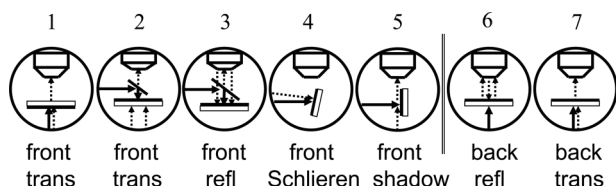


Figure 3. Seven schemes for time-resolved imaging. The solid arrows denote the imaging pulses and the dashed arrows denote the strobe probe pulses. The seven columns in Figs. 6–14 show corresponding results obtained with each scheme. In schemes 1–5 the imaging media is exposed on the coating (front) side, in schemes 6 and 7 on the transparent substrate (back) side.

tor. Then an enable button is pushed which opens the shutter for a single imaging pulse while commanding the computer to save this image only. The shutter is then closed and the sample is translated to a fresh spot for the next image.

As depicted in Fig. 3, seven different imaging schemes¹⁷ were used. The schemes denoted 1–5 involve the imaging pulse incident directly on the coating (“front-side exposure”). Schemes 6 and 7 (“backside exposure”) are possible only for imaging media coated onto transparent substrates. Front- and backside exposure might produce quite different responses for a variety of reasons, including the effects of debris ejected from one surface during exposure and the different distribution of heat in the various layers if the absorber is optically thick. The seven imaging geometries are: scheme 1: front exposure, probe upon coating, transmission image through substrate; scheme 2: front exposure, probe upon substrate, transmission image through pellicle; scheme 3: front exposure, probe upon coating, reflection image; scheme 4: front exposure, probe upon coating, Schlieren image; scheme 5: front exposure, probe upon coating, shadowgraph image; scheme 6: backexposure, probe upon coating, reflection image; and scheme 7: backexposure, probe upon substrate, transmission image.

In schemes 1, 2, and 3 the coating is observed through an aberration inducing intervening optical element, either a thin dichroic pellicle beamsplitter (National Photocolor, Inc.) that reflects the imaging pulses while transmitting the green strobe pulse, or a transparent substrate. In scheme 4, the image is dark unless the coating moves off the substrate and scatters strobe light into the objective to creating a bright image. In scheme 5 the image is bright unless the moving coating shadows the strobe beam. The shiny Ti layer or the glossy substrate surface acts as a mirror, so in schemes 4 and 5 an image and its mirror reflection are observed. The field of view is chosen so that only a small part of the mirror image is seen in the frame at the far left-hand side.

IMAGING MEDIA

The three types of media used here are depicted schematically in Fig. 4. All consist of a poly(ethylene terephthalate) (PET) substrate, an absorber layer and an imaging layer of polydimethyl siloxane [(PDMS) or silicone rubber] [Figs. 4(a) and 4(b)]. The PDMS imaging layer repels ink (oleophobic) and water. Irradiation by a single focused near-IR pulse (typical exposure sources are Nd:YAG or fiber

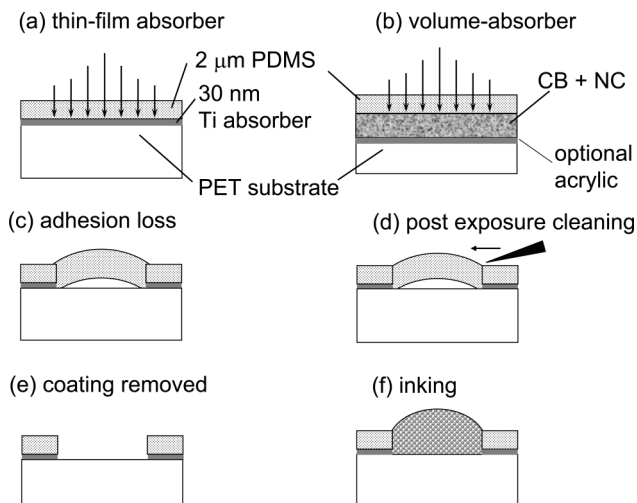


Figure 4. Compositions of imaging media with TF/A, with V/A consisting of carbon black and nitrocellulose (CB+NC), and with V/A/E on PET substrates. The films are imaged when laser pulses heat the absorber layer to a high temperature T_{th} that causes the PDMS coating to debond, creating a well that attracts ink.

lasers in the $1 \mu\text{m}$ wavelength range or diode lasers in the $0.8\text{--}0.97 \mu\text{m}$ wavelength range) causes the PDMS layer to lose adhesion [Fig. 4(c)] to the absorber layer. The exposed region is cleaned with a cloth or brush [Fig. 4(d)], leaving behind an ink-attracting (oleophilic) well [Figs. 4(e) and 4(f)]. Exposing the media to a series of pulses in an image-wise manner creates a plate used for dry offset lithographic printing.^{8,12}

Thin-Film Absorber (TF/A)

We have studied this material (also termed the “basic imaging media”¹⁰) extensively in previous works.^{7–10,16,18,19} As depicted schematically in Fig. 4(a), it consists of a clear PET base with a thin layer Ti absorber deposited by sputtering. The thickness of the Ti layer is adjusted to optimize optical absorption in the near-IR. Measurements of the Ti content are consistent with a layer whose mean thickness is 30 nm. The PDMS imaging layer is deposited with a coverage of 2 g/m^2 for a nominal thickness of $2 \mu\text{m}$.

Volume-Absorbing Media (V/A)

The clear PET base has an adhesion promoting treatment on one side [Fig. 4(b)]. The volume absorber¹¹ coated on this side consists of carbon black in nitrocellulose with a small amount of melamine crosslinker at a coverage of 1 g/m^2 . The PDMS imaging layer again has a nominal thickness of $2 \mu\text{m}$.

Volume/Energetic Media (V/A/E)

These media have the same structure as the volume-absorbing media described above, except an additional energetic layer^{13,21,22} is deposited between the volume absorber and the substrate [Fig. 4(b)]. The energetic layer consists of an acrylic polymer with a melamine crosslinker coated at a coverage of 2.5 g/m^2 . Although we do not think of acrylics as being energetic in the sense of high-energy content self-oxidizing polymers such as nitrocellulose, acrylics are ca-

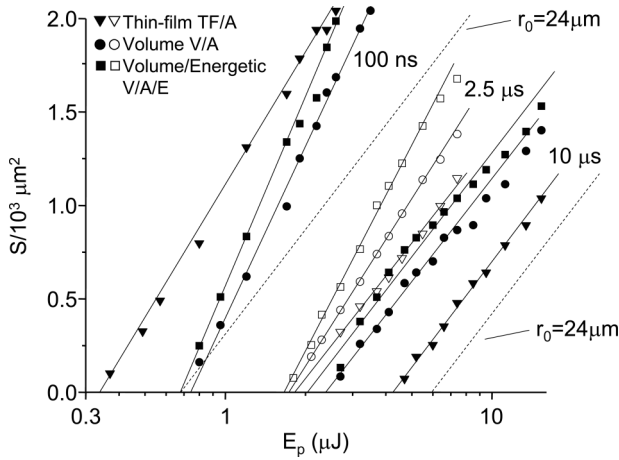


Figure 5. Imaging threshold data for three types of photothermal imaging media using pulse durations 100 ns, 2.5, and 10 μs . The dotted lines have the slope expected for media that obey the local-fluence model. With shorter-duration pulses, the V/A and V/A/E media evidence larger slopes that indicate the presence of useful dot-gain mechanisms at higher pulse energies.

pable of exothermic chemistry and gas evolution in response to heat or shock. In previous work¹⁰ we have shown that with nanosecond laser pulses acrylic underlayers actually generate more hot gas than nitrocellulose.

RESULTS

Imaging Thresholds

Figure 5 summarizes the threshold exposure data for three imaging media with three pulse durations, plotted as imaged area S versus $\log_{10}(\text{pulse energy } E_p)$. These plots are to a good degree linear for all media at all pulse durations. The solid lines in Fig. 5 are linear least-squares fits to the data.

This figure has several interesting features:

1. With the longer-duration pulses, the slopes are quite close to the value predicted by Eq. (3) for a Gaussian beam 24 μm in diameter. The dotted lines in Fig. 5 have the predicted slope.
2. As the pulse duration is decreased, the slope for the TF/A media remains constant, but the slopes for the V/A and V/A/E media increase.
3. The exposure threshold energy E_{th} decreases with increasing laser intensity in such a manner that shorter duration pulses expose imaging media with lower threshold fluences.
4. The TF/A media are the least sensitive with 10 μs pulses but the most sensitive with 100 ns pulses.
5. The V/A/E media are always slightly more sensitive than the V/A media.

Tables I and II summarize these results. Table I lists the laser beam radii extracted from the slopes in Fig. 5. These radii range from 23 to 30 μm , compared to the independently measured value of 24 μm . Of course the laser beam radii would not be affected by the choice of imaging media.

Table I. Laser beam radii (r_0) computed from the slope of exposed spot area versus pulse energy.

	100 ns	2.5 μs	10 μs
Thin-film absorber TF/A	25 μm	22 μm	23 μm
Volume absorber V/A	29 μm	25 μm	23 μm
Volume absorber+energetic V/A/E	30 μm	28 μm	24 μm

Values other than 24 (± 1) μm should be regarded as effective radii that emerge as a result of the dot gain properties of the imaging media.

Table II lists exposure thresholds. The threshold energy E_{th} is the energy where the linear fits intersect the x axis. The threshold J_{th} is computed using Eq. (4), as the ratio $E_{\text{th}}/\text{slope}$. The threshold J'_{th} is computed using the actual beam radius of 24 μm ,

$$J'_{\text{th}} = 2E_{\text{th}}/[\pi \times (24 \mu\text{m})^2]. \quad (5)$$

Time-Resolved Images

A dilemma is what pulse energy to use for the imaging experiments to facilitate interpretations and comparisons. One possibility is to use the same pulse energy for all media and all pulse durations. Another possibility is to always use pulses at the point of greatest efficiency (or some multiple of this pulse energy). With the first choice the more sensitive media will be much further above threshold than the less sensitive media. With the second choice, we will need to compare images obtained with quite different pulse energies. Since we found that pulses somewhat above the point of greatest efficiency provided a richer range of observable behavior, the procedure used here was to find the average J_{th} for all media at a given pulse duration and then fix the pulse energy at a value approximately twice the point of greatest efficiency averaged over the different media. Images obtained with 10 μs pulses used $E_p = 16 \mu\text{J}$, with 2.5 μs pulses $E_p = 9 \mu\text{J}$, and with 100 ns pulses $E_p = 3.5 \mu\text{J}$.

Image streams are presented for three media with three pulse durations in Figs. 6–14. Each image stream was obtained using the seven different geometries described in Fig. 3. Each frame is 170 μm wide by 125 μm tall.

Thin-Film Absorbing Media (TF/A)

Images of the thin-film absorbing media are shown in Figs. 6–8. The Ti layer absorbs $\sim 50\%$ of the incident light, reflects $\sim 30\%$ and transmits $\sim 20\%$. Columns 1, 2, and 7 show transmission images. Comparing columns 1, 2, and 7 shows that the substrate and the pellicle have little adverse effect on the image. The PDMS layer is transparent but the Ti absorber attenuates transmitted light by a factor of about 5, so when the absorber layer melts or boils away, the transmitted light increases by ~ 5 and the images show a bright

Table II. Threshold energies E_{th} and fluences J_{th}

	100 ns			2.5 μ s			10 μ s		
	E_{th} (μ J)	J_{th} (mJ/cm ²)	J'_{th} (mJ/cm ²)	E_{th} (μ J)	J_{th} (mJ/cm ²)	J'_{th} (mJ/cm ²)	E_{th} (μ J)	J_{th} (mJ/cm ²)	J'_{th} (mJ/cm ²)
Thin-film absorber TF/A	0.34	35	38	1.9	250	210	4.3	520	480
Volume absorber V/A	0.74	56	82	1.8	180	200	2.4	290	270
Volume absorber+energetic V/A/E	0.68	48	75	1.7	140	190	2.2	240	240

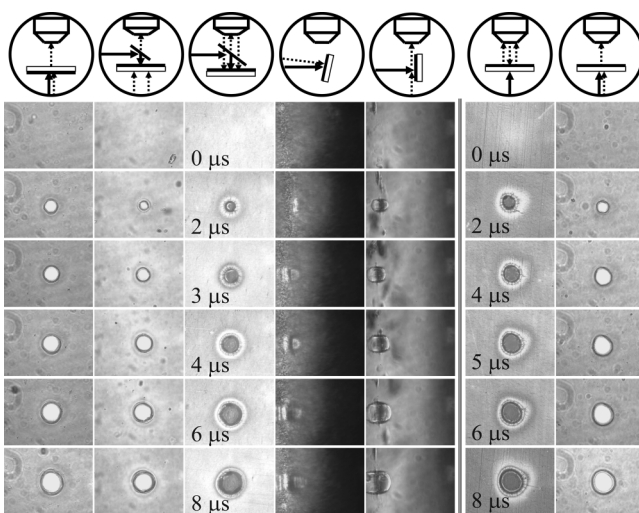


Figure 6. Time-resolved micrographs of the TF/A irradiated by 24 μ m radius 16 μ J pulses of 10 μ s duration. The seven columns represent the seven schemes depicted in Fig. 3. Columns 1–5 use front-face exposure, 6 and 7 use backface exposure. Columns 1, 2, and 7 are transmission images, columns 3 and 6 are reflection images, column 4 is a Schlieren image, and column 5 is a shadowgraph. The image at far left in columns 4 and 5 is an artifact due to mirror-image reflection. Each frame is 170 μ m wide by 125 μ m tall.

spot. Similarly, Ti absorber removal leads to a dark spot in the reflection images in columns 3 and 6, due to loss of mirror reflection.⁷

Microsecond Pulses

In Figs. 6 and 7, the diameter of the bright spot in the transmission images (columns 1, 2, 7) and the dark spot in the reflection images (columns 3, 6) that denotes Ti layer removal grows with time. It takes material at the outer regions of the Gaussian beam a longer time to accumulate enough fluence to melt Ti, so a melt front expands radially as time increases during the pulse. Due to surface tension, the melted Ti recedes outward. The recession of melted Ti with microsecond pulses is apparently fast enough to keep up with the radial expansion of the melt front. The reflection images show a textured annular region in the coating sur-

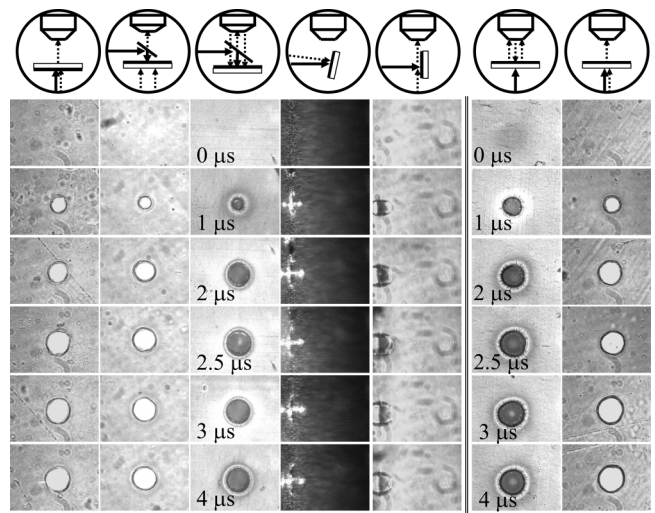


Figure 7. Time-resolved images of the TF/A irradiated by 9 μ J pulses of 2.5 μ s duration. Each frame is 170 μ m wide by 125 μ m tall.

rounding the dark spot. The Schlieren and shadow images (columns 4, 5) show that this region is actually the base of an expanding balloon of PDMS. Recall that a double image is seen in these geometries, so ignore the image of material to the left of the base of the balloon. The volume of the balloon at its maximum is a measure of how much gas has evolved due to thermal decomposition of the PDMS coating at the PDMS-Ti interface. This volume is approximately equal for both 10 and 2.5 μ s pulses, even though E_p is about one-half as much with the shorter pulses. This observation is explained by the thermal conduction model⁹ discussed below.

Nanosecond Pulses

Significantly different behavior is seen in Fig. 8 where nanosecond pulses are used. Figure 8, column 2 at $t=50$ ns indicates that there is boiling or ablation of the Ti layer. Quite a bit more gas is evolved with nanosecond as opposed to microsecond pulses, as seen by the much greater balloon volume in Fig. 8, columns 4, and 5.

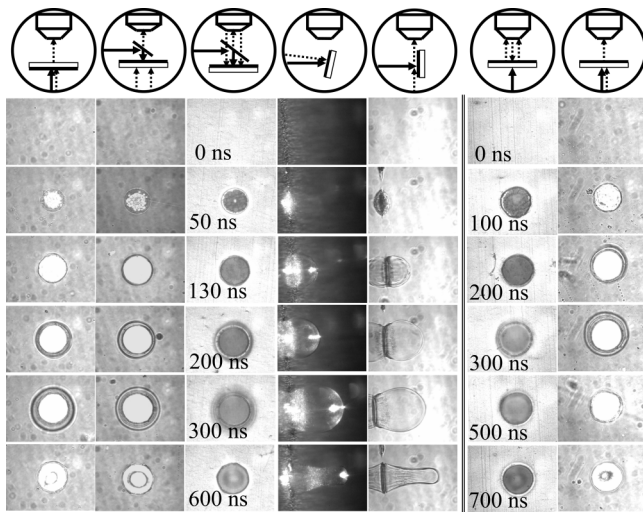


Figure 8. Time-resolved images of the TF/A irradiated by $3.5 \mu\text{J}$ pulses of 100 ns duration. Each frame is $170 \mu\text{m}$ wide by $125 \mu\text{m}$ tall.

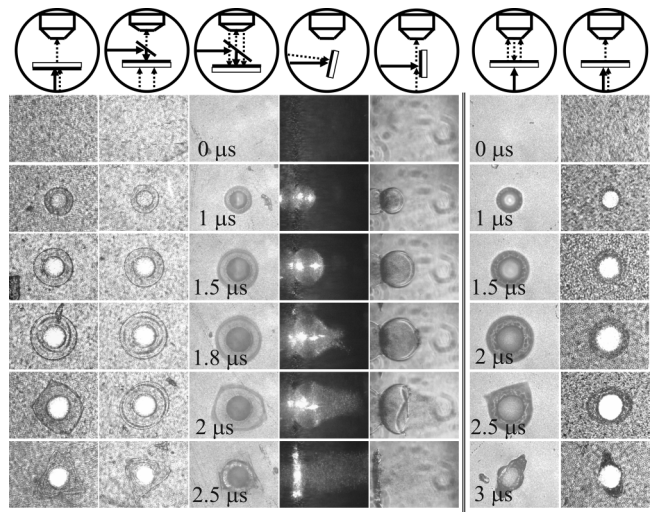


Figure 10. Time-resolved images of the V/A irradiated by $9 \mu\text{J}$ pulses of $2.5 \mu\text{s}$ duration. Each frame is $170 \mu\text{m}$ wide by $125 \mu\text{m}$ tall.

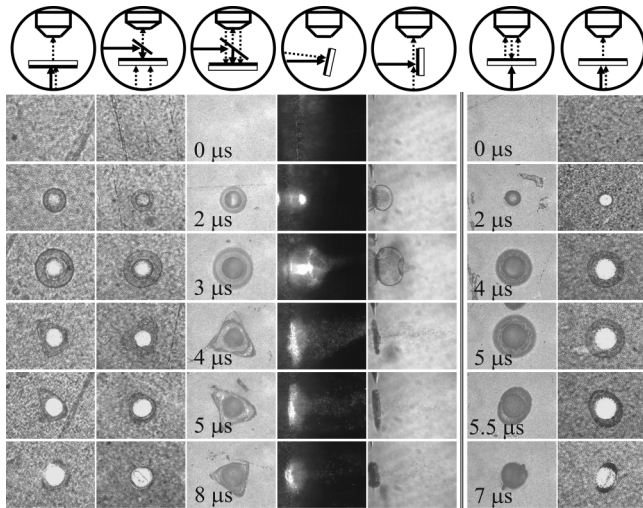


Figure 9. Time-resolved images of the V/A irradiated by $16 \mu\text{J}$ pulses of $10 \mu\text{s}$ duration. Each frame is $170 \mu\text{m}$ wide by $125 \mu\text{m}$ tall.

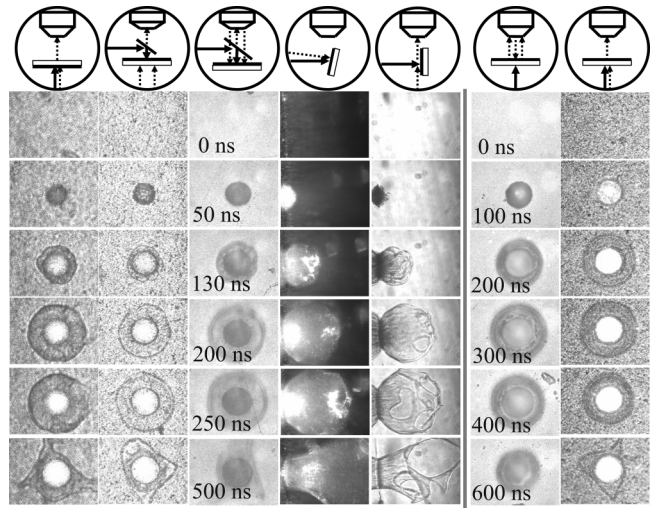


Figure 11. Time-resolved images of the V/A irradiated by $3.5 \mu\text{J}$ pulses of 100 ns duration. Each frame is $170 \mu\text{m}$ wide by $125 \mu\text{m}$ tall.

Volume Absorbing Media (V/A And V/A/E)

With these media, as shown in Figs. 9–14, the absorber layer is black and $\sim 1 \mu\text{m}$ thick. Transmission images (columns 1, 2, 7) see a grainy patina due to the carbon black particles in the absorber. Since the absorber layer is black and it is a poor reflector, its removal is signified by a bright spot in transmission. However, in the reflection images, a dark spot may appear when the shiny PDMS layer begins to balloon even if the absorber layer is still present (e.g., column 3, $t = 50 \text{ ns}$ in Fig. 11).

Microsecond Pulses

As with the TF/A media, with microsecond pulses a bright spot that increases in diameter is seen in transmission in Figs. 9 and 10 and Figs. 12 and 13. However, the bound carbon black layer does not melt and recede. Instead the binder vaporizes and the vapor carries the nonvolatile car-

bon black away, so the expansion of the bright spot is not caused by a receding melt front but by an expanding vaporization zone. The Schlieren and shadow images show that the PDMS balloon expansion is much greater than with the TF/A media. Presumably this is due to extra vapor created by thermal decomposition of the nitrocellulose in the V/A media and the nitrocellulose and acrylic polymers in the V/A/E media not present in the TF/A media. This additional vapor creates an internal pressure that exceeds the bursting strength of the PDMS balloon.¹⁰ A hole is formed in the balloon and the gaseous products escape. Once the balloon bursts, the PDMS layer collapses back onto the substrate. The V/A and V/A/E behavior appears to be quite similar.

Nanosecond Pulses

With nanosecond pulses (Figs. 11 and 14), the volume expansion of the PDMS balloon is much greater than with

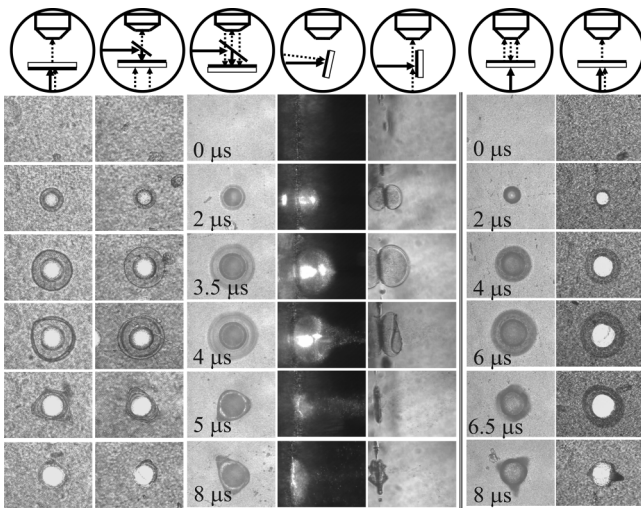


Figure 12. Time-resolved images of the V/A/E irradiated by 16 μJ pulses of 10 μs duration. Each frame is 170 μm wide by 125 μm tall.

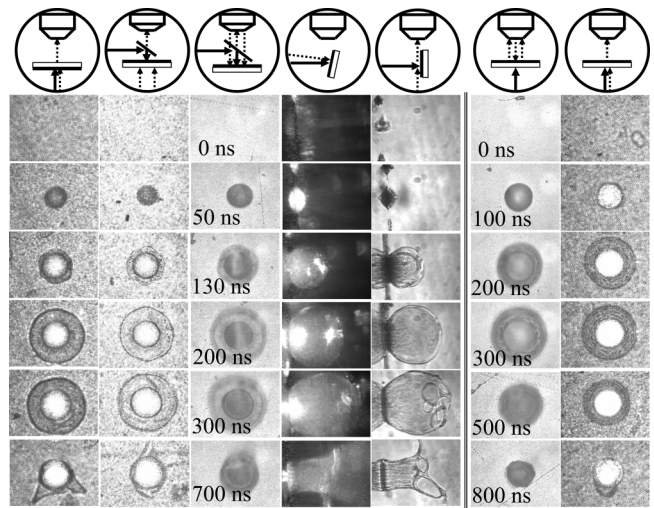


Figure 14. Time-resolved images of the V/A/E irradiated by 3.5 μJ pulses of 100 ns duration. Each frame is 170 μm wide by 125 μm tall.

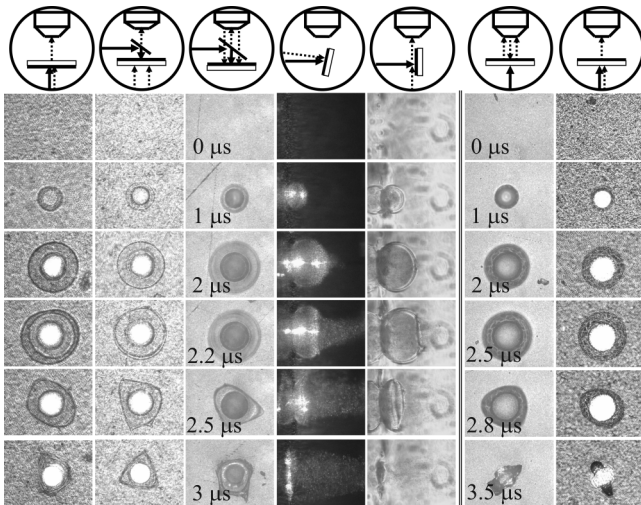


Figure 13. Time-resolved images of the V/A/E irradiated by 9 μJ pulses of 2.5 μs duration. Each frame is 170 μm wide by 125 μm tall.

microsecond pulses. The vapor inside the balloon exceeds the bursting strength by so much that the balloon is literally ripped to shreds.

DISCUSSION

The TF/A medium exhibits a remarkable decrease in J_{th} by a factor of almost 15 as the pulse duration is decreased to 100 ns. The slopes of the S vs E_p lines in Fig. 5 are the same at all pulse durations and are always consistent with the local fluence model so the dot gain is always unity. Thus this material evidences local but nonreciprocal behavior. The exposure mechanism does not change in a fundamental way as the pulse duration is decreased. However, a similar result is observed with less energy input when the pulse duration is shorter, which suggests nonreciprocal behavior results from the dissipative effects of thermal conduction being overcome by the higher intensities of the shorter pulses.⁹ With nano-

second pulses somewhat more gas is evolved, and boiling is observed in the Ti layer, but these effects appear incidental rather than significant. The PDMS balloon never pops. The boiling occurs in the center of the absorber layer where the PDMS coating has already become detached, so it has no effect on the exposure process.

The V/A and V/A/E media show a lesser sensitivity to pulse duration, with J_{th} decreasing by just a factor of 5 in the pulse duration range studied here. The fundamental mechanisms of image formation seem to change as the pulse duration is shortened. With shorter pulses the slopes of the S vs E_p lines in Fig. 5 increase, indicating that dot gain is greater than unity at higher pulse energies in the shorter pulse regime. The time-resolved images associated with this regime show more gas being evolved and the PDMS balloon is observed to expand and burst with increasing violence.

PULSE DURATION (NONRECIPROCAL) EFFECTS

As shown in Table II, all three imaging media become more sensitive as the pulse duration is decreased, but the effect is most dramatic with TF/A media. Using a thermal conduction model developed previously,⁹ we now show that the larger nonreciprocal effect in this medium is a consequence of the relationship between its much thinner absorber layer and the higher laser powers associated with shorter pulse durations. The model was derived using the assumption that a medium becomes imaged when the absorber layer reaches a critical threshold temperature T_{th} .

As depicted in Fig. 15, during laser exposure there is a competition between laser heating and thermal conduction from the absorber layer of thickness Λ_0 into the substrate. A one-dimensional thermal conduction geometry is assumed because $2r_0 \gg \Lambda_0$, that is to say the imaged spot diameter is much greater than the layer thickness.⁹ During a pulse of duration t_p , heat in the absorber layer diffuses into the substrate a distance equal to the thermal diffusion length $\Lambda(t)$,

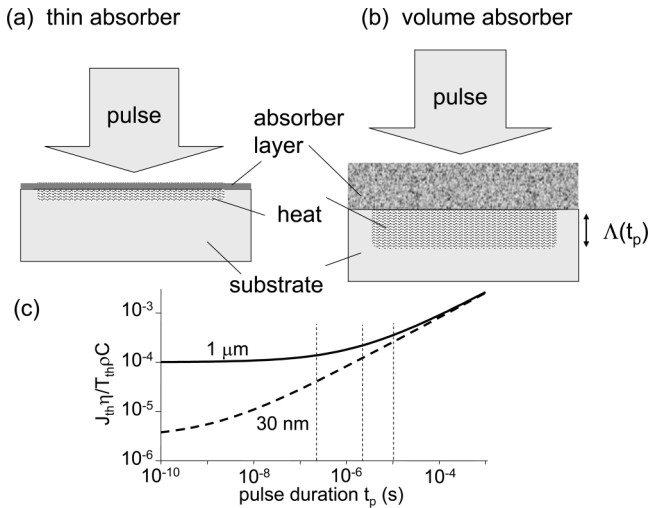


Figure 15. Effects of thermal conduction in (a) imaging media with thinner absorber layer and (b) media with thicker absorber layer. Thermal conduction during a pulse of duration t_p becomes significant when the thermal diffusion length $\Lambda(t_p)$ is comparable to the layer thickness Λ_0 . (c) Calculated dependence of imaging threshold J_{th} on pulse duration t_p for media with a thinner 30 nm absorber and a thicker 1 μm absorber. With the thinner absorber, J_{th} decreases much more below $t_p = 1 \mu\text{s}$. Vertical dotted lines indicate the pulse durations used in the experiments.

$$\Lambda(t) = \sqrt{\pi D t_p}, \quad (6)$$

where D is the substrate thermal diffusivity. The relationship between J_{th} and t_p is given by

$$J_{th} = \frac{T_{th} \rho C}{\eta} (\sqrt{\pi D t_p} + \Lambda_0) = \frac{T_{th} \rho C}{\eta} [\Lambda(t) + \Lambda_0], \quad (7)$$

where η is the fraction of light absorbed and ρ and C are the density and heat capacity of the substrate. In Eq. (7) we have ignored minor corrections resulting from differing thermal properties of the absorber and substrate.⁹

Equation (7) can be used to distinguish two regimes. With shorter duration pulses, $\Lambda(t_p) \ll \Lambda_0$, so thermal diffusion is unimportant and heating is adiabatic. In this regime J_{th} is independent of t_p . At all pulse durations in this regime, the same incident fluence is needed to heat the absorber to T_{th} . With longer duration pulses, $\Lambda(t_p) \geq \Lambda_0$, so during the pulse a significant amount of heat is conducted away from the absorber. In this regime J_{th} increases as $(t_p)^{1/2}$. In this regime more fluence is needed to heat the absorber to T_{th} as the pulse duration is increased. As indicated by Figs. 15(a) and 15(b) and Eq. (7), the boundary between regimes is at the value of t_p where $\Lambda(t_p)$ is about equal to Λ_0 .

The thermal diffusivity⁹ of a PET substrate $D \approx 2 \times 10^{-3} \text{ cm}^2/\text{s}$. Using Eqs. (6) and (7), we can show that $\Lambda(t_p) = \Lambda_0$ when $t_p \approx 1.5 \text{ ns}$ for the 30 nm absorber used in the TF/A media or when $t_p \approx 1.5 \mu\text{s}$ for the 1 μm thick absorber used in the V/A and V/A/E media. Figure 15(c) is a computed plot of J_{th} (in units of $T_{th} \rho C$) versus t_p for a 30 nm absorber and a 1 μm absorber. For the V/A and V/A/E media, J_{th} decreases only gradually below about 1 μs , but with the TF/A media, J_{th} decreases considerably between 2.5 μs and 100 ns. Thus even though in the microsecond

regime the TF/A media has the highest J_{th} , the threshold keeps decreasing at times below 1 μs so that at 100 ns these media become the most sensitive.

DOT GAIN EFFECTS

Dot gain greater than unity refers to imaged spots that are larger in diameter than expected on the basis of the local fluence model. Dot gain should not be viewed as causing an undesirable loss of image resolution, but rather as a desirable increase in sensitivity. With predictable dot gain the point of maximum efficiency moves, but the overall efficiency increases. A laser imaging engine can be designed with appropriate optical elements to focus the laser to the spot size that gives the desired resolution taking into account the dot gain, but a given area will be imaged with less laser energy.

Dot gain is best understood by considering the plots of imaged area S vs E_p in Fig. 5. Dot gain results in a slope increase, most prominently with nanosecond pulses and the V/A or V/A/E media. The effects of dot gain are minimal near threshold, but these effects increase with increasing energy above threshold. For instance, compare the measured response of the V/A/E media with 100 ns pulses to the response predicted by the local fluence model (dashed line in Fig. 5). When the pulse energy is 2.7 times above threshold, the actual imaged area is about twice the value in the local threshold model. In other words the dot gain process here results in an effective threshold lowering of about a factor of two.

Dot gain results from a breakdown of local fluence behavior. As indicated in Fig. 1(a), with Gaussian profile pulses a great deal of energy at the beam center is wasted energy. Any process that transmits this energy from the center outward to where it is needed can increase the efficiency of the imaging process and increase the dot gain. With this background we can identify some strategies to increase the dot gain:

1. Light scattering. Substrate materials with high diffuse reflectivity will scatter the laser energy transmitted through the absorber outward from the beam center.¹⁶
2. Thermal conduction. With longer duration pulses, media design that improves thermal conduction in the plane of the absorber and hinders thermal conduction into the substrate will redistribute the heat in the absorber outward from the beam center.
3. Force transmission. With shorter duration pulses when ablation becomes important, confining the ablated material under a tough outer layer can transmit forces from the beam center to the edges.¹⁰

The materials studied here become imaged when the PDMS coating loses adhesion to the absorber layer. A violent expansion of the PDMS balloon, as seen in Figs. 11 and 14 causes the PDMS layer to pull away from the absorber at the edges.¹⁰ The mechanism of dot gain in this case results from force transmission. Additional forces exerted on the perimeter by excess hot gas at the beam center help expand the

imaged spot. Separation, peeling, or tearing process often depend not only on the applied force but also on the rate of force application. With nanosecond pulses the rate of balloon expansion is about ten times greater than with microsecond pulses.

The dot gain is smaller with the TF/A media because there is less hot gas. The hot gas results primarily from thermal decomposition of the PDMS layer at the absorber interface. Once the PDMS pulls away from the absorber, gas generation stops. With the V/A and V/A/E media the nitrocellulose and acrylic components provide additional sources of gas. Even after the PDMS layer loses adhesion, gas will continue to evolve from these materials. The effects of the nitrocellulose binder appear to be greater than the acrylic underlayer, since there are more dramatic effects in moving from the TF/A media to the V/A media than in moving from the V/A to the V/A/E media.

CONCLUSION

In this paper, we studied the fundamental mechanisms of laser photothermal imaging through a combination of techniques that involved measuring exposure thresholds over a wide range of pulse intensities and pulse durations, and observing the exposure process in real time with time-resolved microscopy in several different observational formats. The results of the threshold measurements are compared to two theoretical models. A local fluence model is used to evaluate the response to Gaussian profile laser beams at a given pulse duration, and a thermal conduction model is used to evaluate the response to changing pulse durations. Deviations from the local fluence model that lead to desirable dot gain properties are identified and the underlying mechanism is revealed from the microscopy experiments.

Some useful findings emerge from this work that can be used to help optimize the design of photothermal imaging materials. Thicker gas-evolving absorber layers appear to be more sensitive than thin-film metallic layers for longer-duration pulses, but with higher intensity lasers that can expose media with shorter duration pulses, the thin-film layers are the best. Desirable dot gain can be realized with a variety of designs, and here the force-transmission mechanism is dominant.

ACKNOWLEDGMENTS

The work performed at the University of Illinois was supported by the US Army Research Office under Award No. W911NF-04-1-0178, the US Air Force Office of Scientific Research under Award No. FA9550-06-1-0235, and the U.S. Department of Energy, Division of Materials Sciences under

Award No. DEFG02-91ER45439, through the Frederick Seitz Materials Research Laboratory at the University of Illinois at Urbana-Champaign.

REFERENCES

- ¹M. L. Levene, R. D. Scott, and B. W. Siryj, "Material transfer recording", *Appl. Opt.* **9**, 2260 (1970).
- ²D. Maydan, "Micromachining and image recording on thin films by laser beams", *Bell Syst. Tech. J.* **50**, 1761 (1971).
- ³W. E. Aas, in *Imaging Processes and Materials*, edited by J. M. Sturge, V. Walworth, and A. Shepp (Van Nostrand Reinhold, New York, 1989), Chap. 13.
- ⁴R. Goulet and D. Fournier, "Workflow as a fundamental motivation for technical evolution", *IS&T's 49th Annual Conference* (IS&T, Springfield, VA, 1996) p. 469.
- ⁵C. DeBoer, "Laser thermal media: The new graphic arts paradigm", *J. Imaging Sci. Technol.* **42**, 63 (1998).
- ⁶I.-Y. S. Lee, W. A. Tolbert, D. D. Dlott, M. M. Doxtader, D. Arnold, D. Foley, and E. R. Ellis, "Dynamics of laser ablation transfer imaging investigated by ultrafast microscopy", *J. Imaging Sci. Technol.* **36**, 180 (1992).
- ⁷S. G. Koulikov and D. D. Dlott, "Time-resolved three-dimensional microscopy of laser photothermal imaging processes", *IS&T's NIP14* (IS&T, Springfield, VA, 1998) Vol. **14**, p. 172.
- ⁸D. E. Hare, S. T. Rhea, D. D. Dlott, R. J. D'Amato, and T. E. Lewis, "Fundamental mechanisms of lithographic printing plate imaging by near-infrared lasers", *J. Imaging Sci. Technol.* **41**, 291 (1997).
- ⁹D. E. Hare, S. T. Rhea, D. D. Dlott, R. J. D'Amato, and T. E. Lewis, "Pulse duration dependence of lithographic printing plate imaging by near-infrared lasers", *J. Imaging Sci. Technol.* **42**, 90 (1998).
- ¹⁰S. G. Koulikov and D. D. Dlott, "Effects of energetic polymers on laser photothermal imaging materials", *J. Imaging Sci. Technol.* **44**, 111 (2000).
- ¹¹E. W. Ellis and F. R. Kearney, U.S. Patent 5,807,658 (1998).
- ¹²T. E. Lewis, M. T. Nowak, K. T. Robichaud, and K. R. Cassidy, U.S. Patent 5,339,737 (1994).
- ¹³T. E. Lewis, M. T. Nowak, and K. T. Robichaud, U.S. Patent 5,353,705 (1994).
- ¹⁴W. A. Tolbert, I.-Y. S. Lee, X. Wen, M. M. Doxtader, E. W. Ellis, and D. D. Dlott, "Laser ablation transfer using picosecond optical pulses: Ultra high speed, low threshold and high resolution", *J. Imaging Sci. Technol.* **37**, 485 (1993).
- ¹⁵W. A. Tolbert, I.-Y. S. Lee, D. D. Dlott, M. M. Doxtader, and E. W. Ellis, "High speed color imaging using laser ablation transfer films with a dynamic release layer: Fundamental mechanisms", *J. Imaging Sci. Technol.* **37**, 411 (1993).
- ¹⁶S. G. Koulikov and D. D. Dlott, "Focus fluctuations in laser photothermal imaging", *J. Imaging Sci. Technol.* **44**, 1 (2000).
- ¹⁷H. Yu, F. R. Kearney, and D. D. Dlott, "Ultrafast three-dimensional microscopy of laser photothermal imaging materials", *Proc. SPIE* **5580**, 24 (2005).
- ¹⁸D. E. Hare, S. T. Rhea, and D. D. Dlott, "New method for exposure threshold measurement of laser thermal imaging materials", *J. Imaging Sci. Technol.* **41**, 588 (1997).
- ¹⁹S. G. Koulikov and D. D. Dlott, "Time-resolved microscopy of laser photothermal imaging", *Opt. Photonics News* **11**, 26 (2000).
- ²⁰S. G. Koulikov and D. D. Dlott, "Ultrafast microscopy of laser ablation of refractory materials: Ultra low threshold stress-induced ablation", *J. Photochem. Photobiol., A* **145**, 183 (2001).
- ²¹E. Ellis, U.S. Patent 5,786,129 (1998).
- ²²T. E. Lewis, M. T. Nowak, and K. T. Robichaud, Eur. Patent EP 0 644 047 B1 (1999).